Supplementary Information for

Long-Range Exciton Diffusion in Two-Dimensional Assemblies of Cesium Lead Bromide Perovskite Nanocrystals

Erika Penzo, Anna Loiudice, Edward S. Barnard, Nicholas J. Borys, Matthew J. Jurow, Monica Lorenzon, Igor Rajzbaum, Edward K. Wong, Yi Liu, Adam M. Schwartzberg, Stefano Cabrini, Stephen Whitelam, Raffaella Buonsanti, and Alexander Weber-Bargioni

S1. PEROVSKITE NANOCRYSTAL (PNC) SAMPLE PREPARATION FOR EXCITON DIFFUSION MEASUREMENTS BY PL MICROSCOPY

Exciton diffusion can be controlled by modulating the NC assembly. Minimizing NC-NC distance (R) is essential to maximizing the rate of FRET (FRET rate is inversely proportional to R^6). In a 3D NC solid, excitons can move in any direction within the solid, as long as the NCs are physically close enough and with sufficient spectral overlap. Confining the NCs to 2D reduces the available paths for exciton hopping to a space directly accessible to imaging by optical microscopy.

The solution concentration and the spinning parameters were optimized for close-packed monolayer deposition; all samples were deposited at 1,500 rpm for 45 seconds and the film morphology was adjusted by varying the concentration of PNCs solution. A closed-packed monolayer without portions of an extra layer and with minimum empty regions was consistently obtained when spin-coating from a *ca.* 3 g/l solution in toluene of $CsPbBr_3$ PNCs at 1,500 rpm for 45 seconds. A sparse monolayer was obtained when spin-coating from a *ca.* 60 mg/l solution of $CsPbBr_3$ PNCs at 1,500 rpm for 45 seconds. A closed-packed monolayer of NCs was not achievable without the surface functionalization with -CH terminated polymer (Supplemental Fig. S1) and/or with solutions in solvents other than toluene. Hexane and octane solutions deposited only patches of multilayers separated by wide empty regions. Development of a reproducible and controllable deposition technique was necessary for establishing consistent PNC monolayers. Simple drop casting, due to the lack of control over the drying process, yielded unacceptable sample-to-sample variability in the final film morphology. Although very effective in forming highly ordered 2D assemblies of conventional semiconducting QDs, methods depending on the interface between immiscible solvents (*e.g.* Langmuir-Blodgett techniques) were not applicable to PNCs because of their instability (solubility) in polar solvents[1]. Spin-coating demonstrated reproducible results and allowed control of the density of PNCs in the film by modulating either spin-coating speed or solution concentration. The morphology of the film was mostly determined by functionalization of the substrate surface and by the solvent in which the PNCs were dispersed. We achieved the best control of film morphology when the substrate surface was functionalized with a -CH terminated polymer and the PNCs were dispersed in toluene. Under these conditions, spin-coating from a dilute solution would yield separated patches of PNCs, with patch sizes controllable all the way to individual PNCs. The distance between individual patches increased as the PNC concentration was reduced. Conversely, deposition from a concentrated solution yielded a continuous monolayer of PNCs, sporadically covered by patches of a second layer. The size of the patches increased, and the distance between them decreased, with increasing solution concentration. For very concentrated PNC solutions, two complete monolayers were formed. The number of layers steadily increases with increasing PNCs concentration in solution, following the same process of patch expansion. The spin-coating speed had a similar effect on film morphology. High spin-coating speeds would reduce the film thickness or increase the spacing between NCs patches and reduce the patches' size, while low spin-coating speed would have the opposite effect. Adjusting the spin-coating speed had a more limited impact on the film morphology. Adjusting the NP concentration was the most effective way to control the PNCs film density. All samples used in this study were screened by SEM to ensure consistent morphologies and to compensate for batch to bath variability common to PNCs.

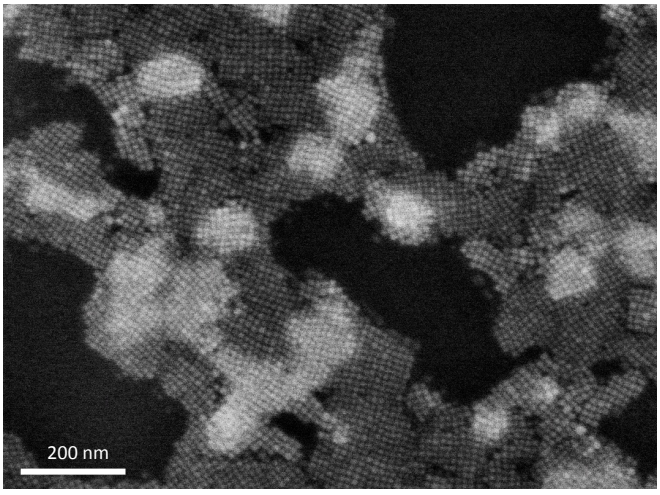

FIG. S1: SEM micrograph of PNCs deposited from a toluene solution (concentration ca. 3 g/l) by spin-coating (1,500 rpm for 45 s) on a Si wafer.

Alumina coating by ALD was necessary to ensure sam-

ple stability under illumination and to prevent long-term degradation due to air moisture. Unprotected PNCs samples were found to be unstable under illumination with a focused laser beam even at low excitation power (below 100 W/cm^2). The main signatures of this instability were a rapid decay of photoluminescence (PL) intensity together with changes in the PNCs film morphology, observed by SEM after exposure to the laser beam.

S2. ESTIMATION OF EXCITON DIFFUSION LENGTH BASED ON GAUSSIAN APPROXIMATION

The average exciton diffusion length of our system can be calculated according to:

$$L_{\text{diff}} = \sqrt{\sigma^2_{\text{diff}} - \sigma^2_{\text{no-diff}}}, \tag{S1}$$

where σ^2_{diff} is the exciton distribution variance in the presence of diffusion (measured on the closed-pack films) and $\sigma^2_{\text{no-diff}}$ is the exciton distribution variance without diffusion (measured on the sparse films). The PL intensity profile measured in a far-field microscopy system is given by the convolution of the single-emitter point spread function (PSF) with the excited-state population density (*i.e.* the exciton distribution). The PL intensity profiles and their underlying excited state population profiles are well approximated by Gaussian functions, so that the additive rule of variances upon convolution applies. The exciton diffusion length as defined above can be determined from the difference in the measured widths of the PL profiles since the effect of the PSF convolution cancels out. The steady-state intensity PL profile was measured on the close-packed and sparse samples repeating the measurement in multiple locations on the same sample and across several samples made from the same solution of PNCs. For each measurement the PL intensity profile was fitted with a Gaussian function and the profile width was extracted as the variance of the Gaussian fit. The two width distributions are shown in Supplemental Fig. S2 for the sparse and close-packed films; their mean values $\langle\sigma^2_{\text{close-packed}}\rangle$ and $\langle\sigma^2_{\text{sparse}}\rangle$ were used to calculate the average exciton diffusion length for our system according to

$$\langle L_{\text{diff}}\rangle = \sqrt{\langle\sigma^2_{\text{close-packed}}\rangle - \langle\sigma^2_{\text{sparse}}\rangle}, \tag{S2}$$

and it was found to be 200 nm.

S3. MODELING EXCITON PROCESSES

This supplement describes in detail the methods we used to model exciton hopping in nanoparticles. We approximated exciton transport within nanoparticle arrays as classical stochastic processes at mean-field (Section S4) and microscopic (Section S5) levels of detail, respectively. In Section S6 we compare simulation results with experiments.

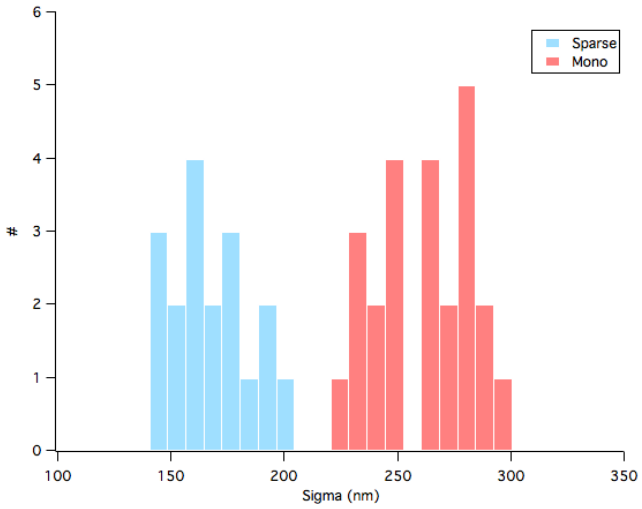

FIG. S2: Histogram of the PL profile sigma measured on a sparse monolayer of PNCs (light blue) and on a close-packed monolayer of PNCs (coral). The average values of the two distributions are (167±18) nm and (260±22) nm respectively.

Readers interested solely in a comparison between the experimental profiles described in the main text and simulated profiles should focus on Section S6. In this section the parameters used in simulations are chosen to match those of our experiments: we consider a square nanoparticle grid of lattice constant 10 nm; a laser source that is an Airy profile of full width half-maximum (FWHM) 240 nm; a laser source intensity low enough that no exciton-exciton interactions occur; a point-spread function for received light that is an Airy profile of FWHM 270 nm; excitons of lifetime ≈ 1 ns; and an exciton hopping rate such that their diffusion constant, on a pristine lattice, is ≈ 0.5 cm^2/s. By contrast, in Section S4 and Section S5, in which we describe in detail the simulation methods used, we use a variety of parameters, chosen for convenience or to make contact with results described in the literature. For instance, we sometimes approximate the laser source to be a Gaussian function, to illustrate differences with the Airy function, or we vary the exciton hopping rate or laser beam intensity in order to illustrate important trends that inform our understanding of the processes under study. We have done this for completeness and to provide the detail required to replicate the results described here.

To summarize, Sections S4 and S5 detail the methods used and make contact with results given in the literature; Section S6 contains the results specific to the present experiments.

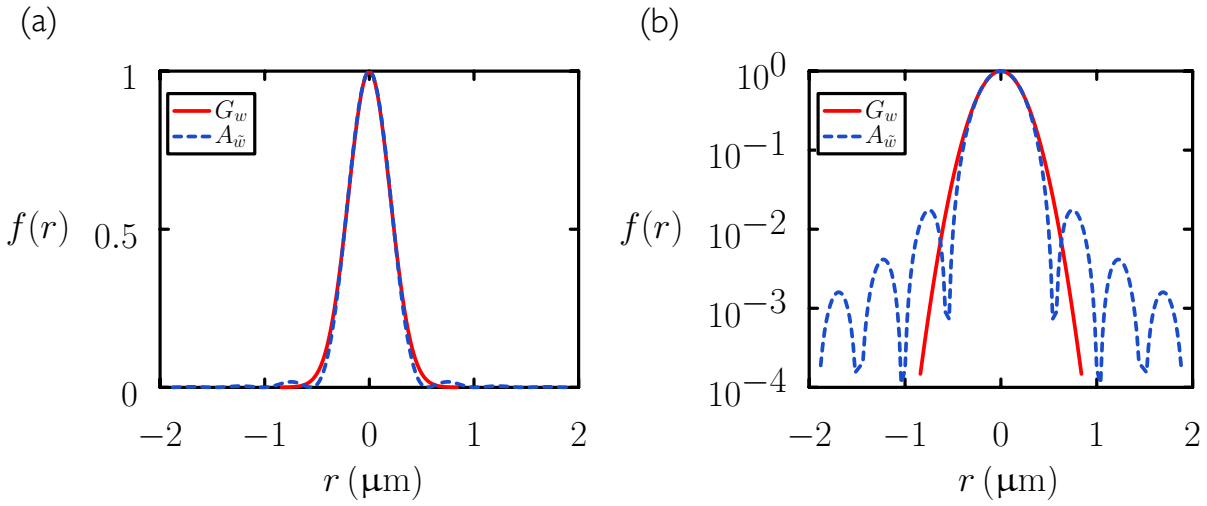

FIG. S3: The Gaussian function $G_w(r)$ and the Airy function $A_{\tilde{w}}(r)$ plotted on linear-linear (a) and linear-log (b) scales ($w = 0.2$ μm). By setting $\tilde{w} \approx 0.728\,w$ we can arrange for the two functions to have equal widths at half their maximum value, and as seen in panel (a) the two functions indeed look similar on that scale. However, panel (b) shows how different the tails of the two functions are. These tails matter to the experiments described in this paper, because the point-spread function of our optics is an Airy function. This function is both the source of radiation 'felt' by the substrate-bound nanoparticles, and is the function convolved with the resulting exciton profile, *via* Eq. (S18), to form the observed profile. When computing the tails of steady-state profiles it is important not to approximate the point-spread function as a Gaussian: see Supplemental Fig. S7.

S4. MEAN-FIELD EQUATIONS

A. Effective description of exciton behavior

The creation, hopping, and recombination of laser-induced excitons in nanoparticles results from the quantum mechanics of light-matter interactions. In this section we approximate these processes by considering the statistics of classical bosonic particles. Consider the diffusion, creation, self-destruction, and pair annihilation of classical bosonic particles on a lattice (see *e.g.* Ref. [2]). Writing down a master equation for this set of processes, taking the continuum steady-state limit, and ignoring fluctuating noise terms, we get

$$D\nabla^2 c(\mathbf{x}) - \mu c(\mathbf{x}) - \rho c(\mathbf{x})^2 = -\Phi(\mathbf{x}). \tag{S3}$$

Here $c(\mathbf{x})$ is the concentration (number per unit area) of particles (excitons) at spatial location $\mathbf{x} = (x, y)$ on a two-dimensional substrate. We shall regard (S3) as an effective steady-state description of the optical signal produced by laser-induced nanoparticle excitons; to do so we make the additional assumption that photons are emitted by isotropic one-body exciton decay, *i.e.* that the optical signal at position $\mathbf{x}$ is proportional to $c(\mathbf{x})$. This description is approximate in several respects, as we shall describe, but several features of its solution, and in particular the approximate shape of the exciton profile produced, provide insight into the workings of our experiments.

The term in (S3) that couples to D describes the diffusion of excitons. This is an approximation: exciton hopping is generally sub-diffusive on small lengthscales and timescales [3]. The term in μ describes the self-destruction of excitons. The term in ρ describes pair annihilation of (bosonic) particles. A similar term (plus higher-order nonlinearities) would also be present in an effective description if particles are instead fermonic (*i.e.* if only one exciton per nanoparticle is permitted). We address this case in Section S5.

The term $\Phi(\mathbf{x})$ describes the intensity of the laser beam at position $\mathbf{x} = (x, y)$ on the two-dimensional substrate. We shall consider profiles with radial symmetry in the plane, and we will write $\Phi(\mathbf{x}) = \Phi_0 f(r/w)$. Here Φ_0 is proportional to the laser power output; $f(r/w)$ is a function containing the laser beam width parameter w; and $r \equiv \sqrt{x^2 + y^2}$ is the radial coordinate. We shall consider cases in which f is an Airy function or its Gaussian approximation. The Airy function is

$$A_w(r) \equiv \left(\frac{2J_1(r/w)}{r/w}\right)^2, \tag{S4}$$

where J_1 is the first-order Bessel function of the first kind. The parameter w quantifies the width of the laser beam. The Gaussian function is

$$G_w(r) \equiv \exp\left(-\frac{r^2}{2w^2}\right). \tag{S5}$$

The functions $G_w(r)$ and $A_{\tilde{w}}(r)$ have equal widths at half their maximum value when $\tilde{w} \approx 0.728\,w$, but differ substantially in their tails; see Supplemental Fig. S3. In this supplement we often use the Gaussian profile for the purposes of illustration. When comparing with experimental data, however, we use the Airy function.

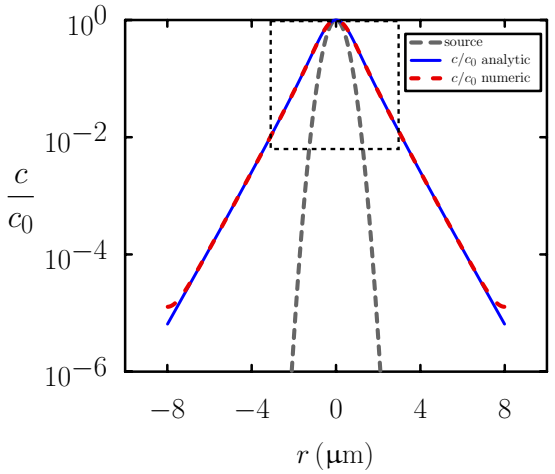

FIG. S4: Numerical (dashed red) [Eq. (S11)] and semi-analytic (blue) [Eq. (S15)] solutions to the linearized version of Eq. (S3) agree, providing a check on our numerical procedure. The parameter combinations are $\mathcal{P} = 0$ and $\mathcal{R}^2 \equiv \mu w^2/D = 0.32$; see Section S4 B. Exciton concentration curves have been normalized by their value at the origin, $c(0) \equiv c_0$. The (normalized) model source is shown grey; for simplicity it is Gaussian with width parameter $w = 0.4$ μm. The dotted box shows the region relevant to typical experimental measurements, in which the measured intensity spans two or three orders of magnitude.

B. Scaling analysis

A scaling analysis shows that (S3) is governed by two parameter combinations. Eq. (S3) can be written

$$\nabla^2 c - \left(\frac{\rho}{D}\right) c^2 - \left(\frac{\mu}{D}\right) c = -\frac{\Phi_0}{D} f\left(\frac{r}{w}\right). \tag{S6}$$

If we choose to measure lengths in units of the beam width w, and introduce coordinates $(\hat{x}, \hat{y}) \equiv w^{-1}(x, y)$, then (S6) becomes

$$\hat{\nabla}^2 c - \left(\frac{\rho w^2}{D}\right) c^2 - \left(\frac{\mu w^2}{D}\right) c = -\frac{\Phi_0 w^2}{D} f\left(\hat{r}\right). \tag{S7}$$

Introducing a rescaled concentration field *via* $c \equiv \left(\Phi_0 w^2/D\right)\hat{c}$ brings (S7) to the form

$$\hat{\nabla}^2 \hat{c} - \mathcal{P}\hat{c}^2 - \mathcal{R}^2 \hat{c} = -f(\hat{r}). \tag{S8}$$

Here we have introduced the parameter combinations

$$\mathcal{P} \equiv \frac{\rho \Phi_0 w^4}{D^2} \tag{S9}$$

and

$$\mathcal{R}^2 \equiv \frac{\mu w^2}{D}. \tag{S10}$$

The combination $\mathcal{P} \equiv \rho\Phi_0 w^4/D^2$ is the nonlinearity or power parameter. When $\mathcal{P}$ is large the beam is powerful in the sense that the term nonlinear in c is important. When $\mathcal{P}$ is small we are in the linear regime, where the term in ρ in Eq. (S3) may be ignored. The experiments reported in this paper are performed in the linear regime.

The parameter $\mathcal{R} \equiv \sqrt{\mu w^2/D}$ is a ratio of lengthscales. $\ell_{\mathrm{beam}} \equiv w$ is the lengthscale associated with the beam profile. $\ell_{\mathrm{hop}} \equiv \sqrt{D/\mu}$ is the lengthscale on which an exciton that lives for characteristic time μ^{-1} will hop before it dies. Thus when $\mathcal{R} = \ell_{\mathrm{beam}}/\ell_{\mathrm{hop}}$ is large, the beam diameter is much greater than the distance over which a typical exciton will diffuse. When $\mathcal{R}$ is small, the beam diameter is much less than the exciton hopping distance. For the experiments reported in the main text the lengths ℓ_{beam} and ℓ_{hop} are comparable.

C. Numerical solution of Eq. (S3)

In general, Eq. (S3) must be solved numerically. To do so we simulated numerically the time-dependent version of the equation on a 2D periodic grid, using a forward-different method and a five-point Laplacian stencil:

$$\begin{aligned} c_{x,y}(t+\Delta t) &= c_{x,y}(t) + \Delta_t\left[-\rho c_{x,y}(t)^2 - \mu c_{x,y}(t) + \Phi_0 f(r\Delta_x^{-2}/w)\right] \\ &+ D\Delta_t\Delta_x^2\left[c_{x+1,y}(t) + c_{x-1,y}(t) + c_{x,y+1}(t) + c_{x,y-1}(t) - 4c_{x,y}(t)\right]. \end{aligned} \tag{S11}$$

Here $c_{x,y}(t)$ is the exciton concentration at grid point (x, y) at time t. We measured spatial distances in microns, and took $\Delta_x = 50$ (*i.e.* we have 50 lattice spacings to the micron). We set the timestep $\Delta t = 10^{-5}$, which was small enough to maintain numerical stability. We usually began simulations with a spatial profile $c(r)$ equal to that of the source term $\Phi_0 f(r\Delta_x^{-2}/w)$, and simulated until the steady state was reached. We confirmed the accuracy of our numerics by comparing the steady-state solution of Eq. (S11) to a semi-analytic solution of Eq. (S3) in a certain limit (Section S4 D): see Supplemental Fig. S4.

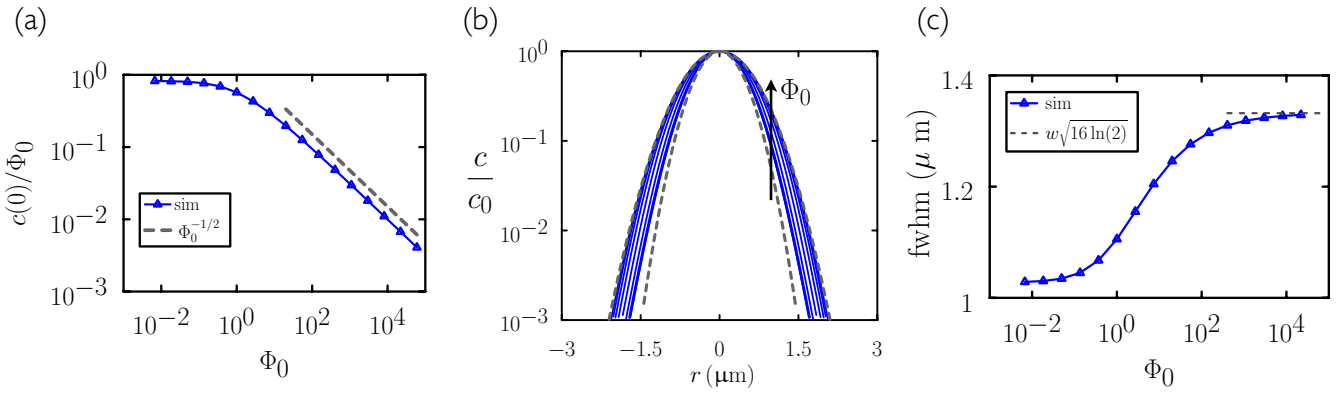

FIG. S5: Numerical solutions to Eq. (S3) for a range of source intensities Φ_0 show that the scale and shape of profiles change as we move from the linear to the nonlinear regime. For the purposes of illustration we consider a Gaussian source with width parameter $w = 0.4$ µm. (a) The maximum exciton concentration changes dependence upon Φ_0 upon moving from the linear to the nonlinear regime. (b) The profile widths tend towards the square root of the souce profile (the outer dotted line) in the large-Φ_0 limit. (c) The full widths at half-maximum value (FWHM) of the profiles change accordingly. Equation parameters: the lengthscale parameter combination (S10) is $\mathcal{R} \equiv \mu w^2/D = 8$, indicating that the source width is greater than the exciton diffusion length (and so low-power profiles are only slightly broader than the source). The power parameter (S9) is $\mathcal{P} = 64\Phi_0$, which must be much smaller than unity to be in the linear regime.

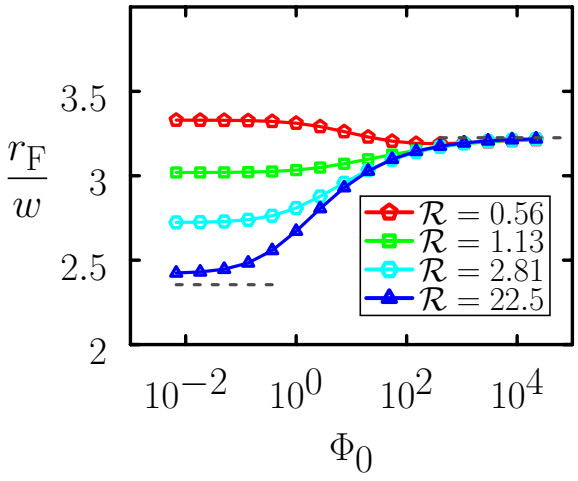

FIG. S6: The full width at half maximum r_F of a series of normalized exciton profiles, plotted relative to the source width w (= 0.15 µm), for a range of source intensities Φ_0. Distinct curves correspond to distinct choices of exciton diffusion constant D; the resulting dimensionless parameters $\mathcal{R} \equiv w^2\mu/D$ are shown. The dotted lines left and right indicate the width of the source and $\sqrt{2}$ times that value, respectively. The smaller is $\mathcal{R}$ the broader is the exciton profile in the linear (small-Φ_0) regime. At large Φ_0, in the strongly nonlinear regime, all profile widths tend to a value $\sqrt{2}$ times that of the source. Whether nonlinear broadening or narrowing occurs depends therefore on the value of $\mathcal{R}$.

D. Semi-analytic solution of the linearized version of Eq. (S3)

As a benchmark for our numerics (Section S4 C) and to gain insight into the properties of Eq. (S3), it is instructive to solve the equation in the absence of the term in ρ, *i.e.* in the linear limit. The linear limit is appropriate when the source intensity Φ_0 and the resulting maximum exciton concentration is small.

In 2D the solution of Equation (S3) can be obtained by the method of Green's functions, and is

$$c(x,y) = \frac{\Phi_0}{2\pi D}\int_{-\infty}^{\infty}\mathrm{d}y'\int_{-\infty}^{\infty}\mathrm{d}x'\Phi\left(\sqrt{(x')^2+(y')^2}\right) \times K_0\left(\lambda\sqrt{(x-x')^2+(y-y')^2}\right). \quad \text{(S12)}$$

Here $\lambda \equiv \sqrt{\mu/D}$ is the reciprocal of the characteristic lengthscale for exciton diffusion, and K_0 is the zeroth order modified Bessel function of the second kind. Writing $u \equiv x - x'$ and $v \equiv y - y'$, and passing to plane polar coordinates *via* the transformations $(u,v) = \xi(\cos\theta', \sin\theta')$ and $(x,y) = r(\cos\theta, \sin\theta)$ gives

$$c(r,\theta) = \frac{\Phi_0}{D}\int_0^{\infty}\xi\mathrm{d}\xi K_0(\lambda\xi) \quad \text{(S13)}$$
$$\times \int_0^{2\pi}\frac{\mathrm{d}\theta'}{2\pi}\Phi\left(\sqrt{r^2+\xi^2+2r\xi\cos(\theta-\theta')}\right).$$

The source Φ in our experiments is an Airy function, but for the purposes of checking our numerics we replace it by a Gaussian function. In this case (S13) can be reduced to a single integral. Setting $\Phi(r) = \Phi_0 \mathrm{e}^{-(x^2+y^2)/(2w^2)}$ we have

$$c(r,\theta) = \frac{\Phi_0}{D}\mathrm{e}^{-r^2/(2w^2)}\int_0^{\infty}\mathrm{d}\xi\,\xi\mathrm{e}^{-\xi^2/(2w^2)}K_0(\lambda\xi) \times \int_0^{2\pi}\frac{\mathrm{d}\theta'}{2\pi}\mathrm{e}^{r\xi w^{-2}\cos(\theta-\theta')}. \quad \text{(S14)}$$

The inner integral can be carried out using the formula $\int_0^{2\pi}\mathrm{d}\theta\,\exp(\alpha\cos\theta+\beta\sin\theta) = 2\pi I_0(\sqrt{\alpha^2+\beta^2})$, where

I_0 is the zeroth-order modified Bessel function of the first kind. This result allows us to write (S14) in the manifestly θ-independent form

$$c(r) = \frac{\Phi_0}{D}\mathrm{e}^{-r^2/(2w^2)} \times \int_0^\infty \mathrm{d}\xi\, \xi \mathrm{e}^{-\xi^2/(2w^2)} K_0(\lambda\xi)\, I_0\left(\frac{r\xi}{w^2}\right), \quad \text{(S15)}$$

which we can evaluate numerically. In Supplemental Fig. S4 we show that, in the relevant parameter regime, the steady-state limit of the numerical procedure (S11) agrees with the semi-analytic solution (S15), except near the edge of the simulation box (where artifacts associated with periodic boundaries are apparent). The dotted square shows the scale on which we typically compare our simulations with experimental data, which is well away from such artifacts.

Note that rescaling space and the concentration field in the manner described in Section S4 B confirms that (S15) depends only upon the single parameter combination $\mathcal{R} \equiv \sqrt{\mu w^2/D}$:

$$\hat{c}(\hat{r}) = \mathrm{e}^{-\hat{r}^2/2} \int_0^\infty \mathrm{d}\hat{\xi}\, \hat{\xi} \mathrm{e}^{-\hat{\xi}^2/2} K_0\left(\hat{\xi}\mathcal{R}\right) I_0\left(\hat{r}\hat{\xi}\right). \quad \text{(S16)}$$

E. Interpolation between linear and nonlinear regimes

When the nonlinear term is present in Eq. (S3), the shape of the exciton profile changes with source power Φ_0. Consider a Gaussian source of width w, $\Phi(r) = \Phi_0 G_w(r)$ [see Eq. (S5)]. When Φ_0 is large, such that the parameter combination $\mathcal{P} \equiv \rho\Phi_0 w^4/D^2 \gg 1$, Eq. (S3) can be approximated near its core as

$$\rho c^2 = \Phi_0 G_w(r), \quad \text{(S17)}$$

from which we get $c(0) \propto \Phi_0^{1/2}$. Thus, as shown in Supplemental Fig. S5(a), plotting $c(0)/\Phi_0$ for a series of numerical experiments carried out at different source intensities Φ_0 indicates the onset of the nonlinear regime. The value of the gradient of the function in the high-power regime depends on the types of nonlinearities present (*e.g.* it differs for bosonic and fermionic excitations), but the qualitative change can be used to determine the extent of the linear regime.

As we move from the linear to the nonlinear regime, the width of the exciton profile changes. In the linear regime the width of the exciton profile is determined (for the model diffusion equation) by the source width w and the decay length $\sqrt{D/\mu}$. In Supplemental Fig. S5(b) we show a series of normalized exciton profiles (blue) that result from (S3), for the range of choices of source power Φ_0 shown in panel (a). In (b), the inner profile corresponds to the case of lowest power, and is slightly larger than the source (the inner dotted gray line) by virtue of the diffusive broadening seen in Supplemental Fig. S4. As source intensity increases, the profiles broaden. From Eq. (S17) we see that in the limit of large intensity, the spatial profile has the shape $c(r) \propto G_w(r)^{1/2} = G_{w\sqrt{2}}(r)$, which is a Gaussian with a width $\sqrt{2}$ times that of the source. As shown in Supplemental Fig. S5(b), the outer blue profiles indeed tend to this shape (shown by the outer dotted gray line). Plotting profiles' full width at half maximum value in Supplemental Fig. S5(c), we see that they tend to the expected width in the limit of large Φ_0.

Nonlinear *narrowing* can also be seen, when the decay length $\sqrt{D/\mu}$ is large compared with the source width w. In this case the dimensionless parameter $\mathcal{R} < 1$, and the profile width in the linear regime can be broader than the profile width in the strongly nonlinear regime, which tends to a value $\sqrt{2}$ times that of the source; see Supplemental Fig. S6. Note that these width comparisons refer to shapes of *normalized* profiles, those scaled by their values $c(0)$ at the origin: profiles generated at large values of Φ_0 are generally broader than those generated at small Φ_0, in the sense that greater exciton density is generated away from the origin.

F. Observed profiles are a convolution of the exciton profiles and the optics' point-spread function

Intensity profiles $I(r)$ observed in experiment are not the exciton profiles $c(r)$ themselves, but are instead the convolution of the exciton profile and the point-spread function $S(r)$ of the optics [3]:

$$I(r) = (c \star S)(r) = \int \mathrm{d}x'\mathrm{d}y' c(x',y') S(x-x', y-y'). \quad \text{(S18)}$$

The optics plays a dual role in our experiments: it gives rise to an Airy-function source profile $\Phi(r)$ of FWHM 240 nm on the substrate, and it gives rise to the point-spread function $S(r)$ for received light, an Airy function of FWHM 270 nm, that appears in (S18). Airy functions are sometimes approximated as Gaussian functions, because the cores of the two profile types have similar shapes [Supplemental Fig. S3(a)]. However, the tails of the two functions differ markedly [Supplemental Fig. S3(b)]. This difference is significant when computing steady-state profiles, as shown in Supplemental Fig. S7, particularly as regards inflation of the tail of the profile. We carried out the convolution (S18) numerically.

The trends described previously, such as the broadening of profiles at large source power, can be seen in $I(r)$ much as in $c(r)$, with quantitative differences: see *e.g.* Supplemental Fig. S8.

S5. MICROSCOPIC SIMULATIONS

To complement the approach of Section S4 we simulated space-dependent exciton dynamics using discrete-

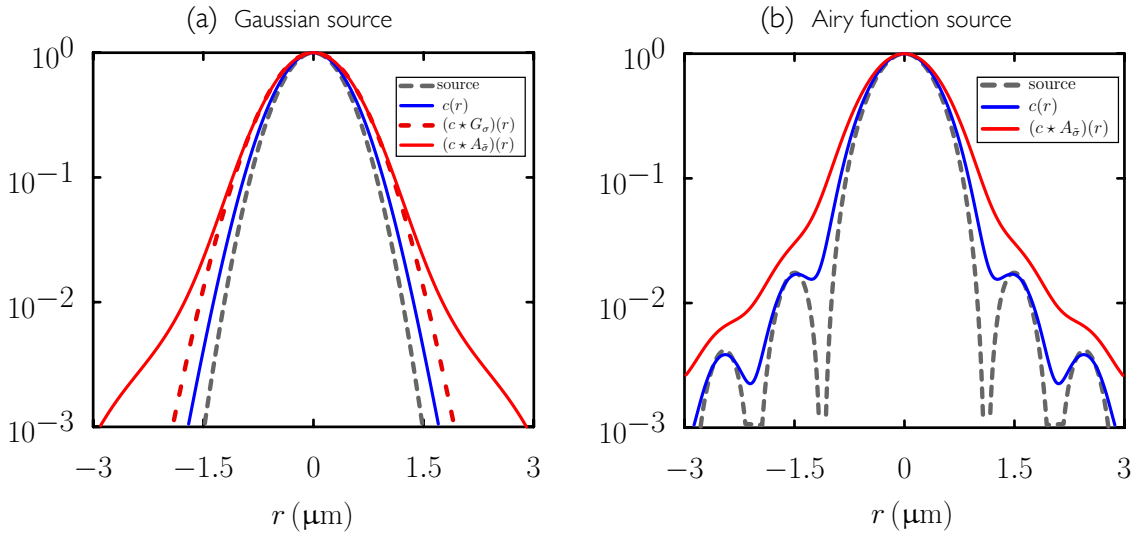

FIG. S7: Gaussian and Airy functions used for the source profile $\Phi(r)$ and the convolution (S18). (a) Numerical solution to Eq. (S3) for a Gaussian source $\Phi(r) \propto G_\sigma(r)$ of width $\sigma = 0.4$ µm (gray dotted) gives an exciton profile $c(r)$ (blue). Subsequent convolution with a Gaussian (red dotted) or an Airy function (red solid) produce distinct curves. (b) Numerical solution to Eq. (S3) for an Airy function source $\Phi(r) \propto A_{\tilde\sigma}(r)$, with $\tilde\sigma = 0.7\sigma$ (gray dotted), gives an exciton profile $c(r)$ (blue) whose tails are markedly different to the tails of $c(r)$ with a Gaussian source. Subsequent convolution with an Airy function gives the solid red line.

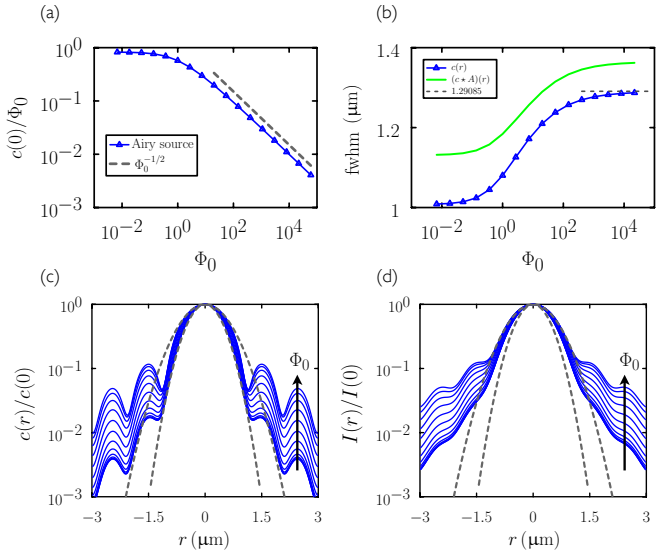

FIG. S8: Observed profiles $I(r)$ vary in a similar fashion to exciton profiles $c(r)$, with quantitative differences. (a) Similar to Supplemental Fig. S5(a), but with an Airy-function source of width 0.24 µm. (b) The full width at half maximum (FWHM) of exciton- and observed profiles behaves similarly, but are numerically different. Profiles $c(r)$ and $I(r)$ are shown in (c) and (d), respectively, overlaid on Gaussian reference curves.

time and continuous-time Monte Carlo algorithms.

A. Fermionic statistics

We consider a two-dimensional substrate of nanoparticles whose positions are fixed. In Section S6 we take the nanoparticles to sit in a square array, similar to the experiments reported in the main text; in this section we also consider trangular arrays and disordered arrangements. We model excitons as classical particles, able to undergo various processes. Each nanoparticle can be occupied by an exciton A or be vacant $\emptyset$, *i.e.* we assume fermionic exciton statistics. In this case the normalized exciton profiles broaden at high power even in the absence of exciton hopping. The broadening is different in detail to that of the bosonic statistics considered in Section S4. Consider exciton creation with rate $\Phi(r)$,

$$\emptyset \xrightarrow{\Phi(r)} \mathrm{A}, \tag{S19}$$

where $\Phi(r) = \Phi_0 f(r)$ is the laser source as in Section S4, and exciton self-destruction with rate μ,

$$\mathrm{A} \xrightarrow{\mu} \emptyset. \tag{S20}$$

The stochastic process defined by (S19) and (S20) is a two-state dynamics with steady-state solution

$$c(r) = \frac{\Phi(r)}{\Phi(r) + \mu}, \tag{S21}$$

where $c(r)$ is the density of excitons (A-particles) at position r. We assume that the process of destruction produces a photon, and so the time-averaged exciton density

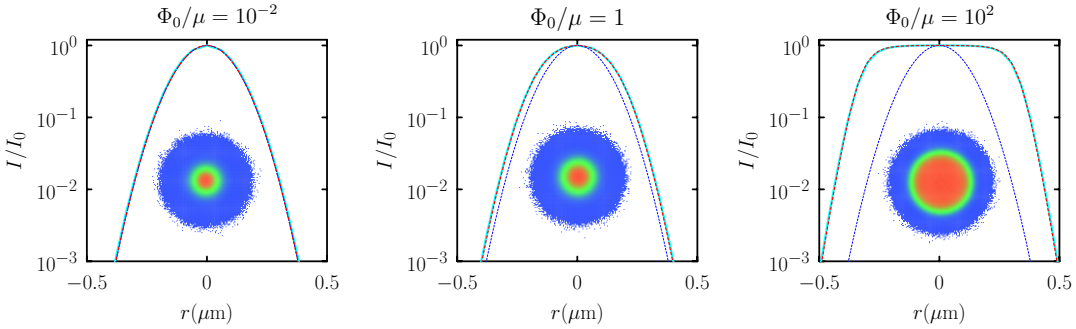

FIG. S9: Numerically computed steady-state radial exciton profiles $c(r)$ (cyan) and the exact solution (S21) (red dashed) for the processes (S19) and (S20), together with the model Gaussian source profile (blue dotted). Shown inset are the two-dimensional images from which the radial profiles are computed.

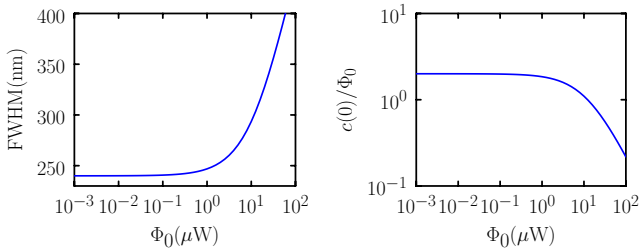

FIG. S10: FWHM (left) and normalized intensity (right) of exciton profiles $c(r)$ produced by the stochastic processes (S19) and (S20), for varying beam power Φ_0. We take $\mu = 0.5\,\mathrm{ns}^{-1}$. Note that the FWHM continues to broaden with source power, unlike the case of bosonic exciton statistics.

is proportional to the steady-state photoluminescence intensity.

We simulated these processes using continuous-time Monte Carlo [4] and a square-lattice nanoparticle array. Comparison with (S21) provides a simple benchmark against which to check the calculation of radially-averaged profiles. As shown in Supplemental Fig. S9, the time- and radially-averaged profile $c(r)$ is proportional to the source profile $\Phi(r)$ at low power, and broadens as beam power is increased. For the purposes of illustration we take the source $\Phi(r) = \Phi_0 G_w(r)$ to be Gaussian with full width at half maximum intensity (FWHM) 240 nm, *i.e.* $w = (120/\sqrt{2\ln 2})\,\mathrm{nm}$.

For fermionic statistics the width of the profile grows logarithmically with power at high power: we can solve the equation $c(r_0) = c(0)/2$ to yield the FWHM, $F \equiv 2r_0$:

$$F(\Phi_0) = 2w\sqrt{2\ln\left(\frac{\Phi_0}{\mu}+2\right)}. \qquad \text{(S22)}$$

We can also calculate the total integrated intensity

$$I_{\mathrm{tot}} = \int \mathrm{d}\theta\, r\mathrm{d}r\, c(r) = 2\pi w^2 \ln\left(\frac{\mu+\Phi_0}{\mu}\right), \qquad \text{(S23)}$$

for Gaussian $\Phi(r)$. We have $I_{\mathrm{tot}} \approx 2\pi w^2 \Phi_0/\mu$ for small Φ_0/μ. Equations (S22) and (S23) are plotted in Supplemental Fig. S10. We take the rate of self-destruction to be $\mu = 0.5\,\mathrm{ns}^{-1}$ and the beam power parameter to be $\Phi_0 = (P/24.4)\,\mathrm{ns}^{-1}$, where P is measured in microwatts (μW), which we estimate to be characteristic of our experiments. These behaviors are useful diagnostics of the onset of nonlinear behavior, and allow us to verify that experiments reported in the main text are done in the linear regime.

B. Exciton hopping is subdiffusive in the presence of energetic disorder

In the experiments reported in the main text we believe that subdiffusive motion of excitons arises from vacancies in the nanoparticle array. In this section we recall some features of exciton subdiffusion brought about by another mechanism, energetic disorder, that has been quantified in other studies [3]. Hopping on a rough energy landscape leads in general to subdiffusive behavior at short times and diffusive behavior at long times [5, 6].

To make contact with these results we carried out Monte Carlo simulations of an exciton moving between nanoparticles on a two-dimensional substrate; see Supplemental Fig. S11. Simulation boxes had periodic boundaries in both dimensions. We considered spatially ordered substrates, in which nanoparticles were arranged as a close-packed lattice with inter-particle separation $a = 8$ nm – see Supplemental Fig. S11(a) – and spatially disordered substrates, such as that shown in Supplemental Fig. S11(b). These we generated by performing short constant-volume Monte Carlo simulations of the nanoparticles themselves, assuming they were hard discs with radii drawn from a truncated Gaussian distribution peaked about 8 nm. We found (shown below) that at constant particle density the averaged exciton transport properties were not strongly affected by the presence of spatial disorder.

Once the substrate was generated, we performed ex-

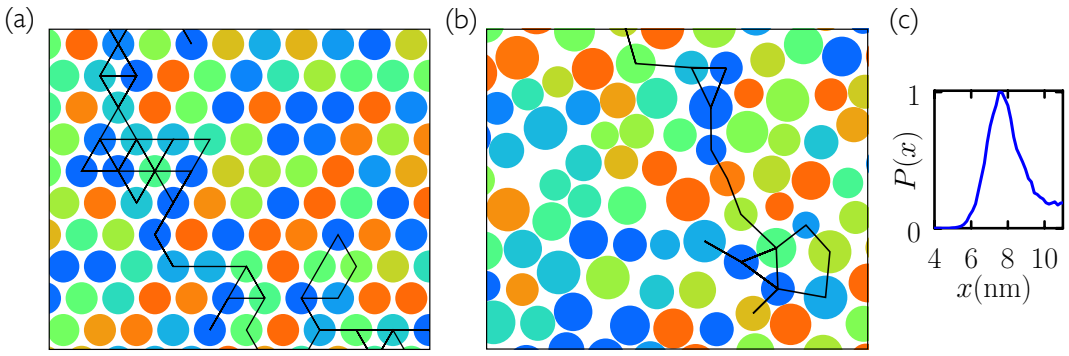

FIG. S11: Examples of spatially ordered (a) and disordered (b) substrates used for illustrative exciton-hopping simulations. The black traces show trajectories taken by two simulated excitons. Nanoparticle colors indicate their energies; red shades and blue shades are high and low in energy, respectively. Panel (c) shows the distribution of inter-nanoparticle distances seen in panel (b).

citon hopping simulations using a discrete-time Monte Carlo algorithm. We selected at random a nanoparticle, and created an exciton on that nanoparticle. We then selected at random any neighbor (up to a cutoff distance) of that nanoparticle, and proposed to move the exciton to that nanoparticle. Following Ref. [7] we accepted this proposal with a probability designed to ensure that the exciton jump from i to j happens with rate

$$R(i \to j) = \frac{1}{\tau_0} \left(\frac{R_0}{R_{ij}} \right)^6 \min \left(1, \mathrm{e}^{-\beta(E_j - E_i)} \right). \quad \text{(S24)}$$

Here i and j are the nanoparticle identities; τ_0 is the mean exciton lifetime; R_0 is the Förster radius; R_{ij} is the distance between nanoparticles i and j; E_i and E_j are the bandgaps of nanoparticles i and j; and $\beta \equiv (k_\mathrm{B}T)^{-1}$. For spatially disordered substrates the combination R_0/R_{ij} can be greater than or less than unity, and so it is convenient to write (S24) as

$$R(i \to j) = \frac{1}{\tau} \left(\frac{R_\mathrm{min}}{R_{ij}} \right)^6 \min \left(1, \mathrm{e}^{-\beta(E_j - E_i)} \right), \quad \text{(S25)}$$

with $R_\mathrm{min} \equiv \min_{ij} R_{ij}$ and $\tau \equiv \tau_0 \left(R_\mathrm{min}/R_0 \right)^6$. With time measured in units of τ we accepted the move from i to j with probability

$$p_\mathrm{acc}(i \to j) = \left(\frac{R_\mathrm{min}}{R_{ij}} \right)^6 \min \left(1, \mathrm{e}^{-\beta(E_j - E_i)} \right), \quad \text{(S26)}$$

which is ≤ 1. Otherwise, the proposed exciton move was rejected. We considered a Gaussian distribution of nanoparticle energy levels E_i with variance ϵ^2, $P(E_i) \propto \exp\left(-E_i^2/(2\epsilon^2)\right)$.

The exciton diffusion parameter is

$$D(t) = \frac{\langle [\Delta x(t)]^2 \rangle + \langle [\Delta y(t)]^2 \rangle}{4 N_\mathrm{steps}} \cdot \frac{a^2}{\tau_0} \left(\frac{R_\mathrm{min}}{R_0} \right)^6, \quad \text{(S27)}$$

where $\Delta x(t)$ and $\Delta y(t)$ are the time-dependent distances (in units of a) traveled in each dimension by excitons (corrected for periodic boundaries); averages $\langle \cdot \rangle$ are taken over initial conditions, waiting times and (where appropriate) realizations of energetic and spatial disorder; and N_steps is the number of Monte Carlo steps taken. Simple considerations indicate roughly the exciton diffusion constant expected. Take the nanoparticle radius to be $a \sim 10$ nm. Assume the characteristic rate for an exciton to hop from nanoparticle to nanoparticle is $\tau_0^{-1}(R_0/a)^6$, where $\tau_0 \sim 10$ ns, and assume that the Förster radius R_0 is of order 10 nm [3]. Then the long-time exciton diffusion constant is roughly $D = \frac{1}{2\tau_0} \left(\frac{R_0}{a} \right)^6 a^2 \approx 10^{-4}$ cm^2/s. This scale of this result is consistent with the exciton diffusion constant of 3×10^{-4} cm^2/s reported in Ref. [3]; the precise numerical value of this result is sensitive to the ratio R_0/a to the sixth power, and upon insertion of different values (*e.g.* $R_0 = 12.5$ nm and $a = 8$ nm) we obtain the numbers shown in Supplemental Fig. S12(a).

In that figure we show D from Eq. (S27), as a function of time, for four different values of energetic disorder (on a spatially uniform lattice). A constant value indicates diffusive motion, which is reached at times that increase as the roughness $\epsilon/(k_\mathrm{B}T)$ of the energy landscape increases. For *e.g.* nanoparticles for which $\epsilon \approx k_\mathrm{B}T$, we estimate the diffusive approximation made in Eq. (S3) to be valid only on timescales exceeding about 100 ns [in general the D appearing in (S3) could be thought of as a spatial and temporal average over the microscopic behavior shown in Supplemental Fig. S12(a)].

In Supplemental Fig. S12(b) we show the long-time diffusion constant obtained for particular values of substrate energetic disorder, normalized by the value for no energetic disorder. For a spatially ordered lattice (green line), the fall-off of D with $\epsilon/(k_\mathrm{B}T)$ is less rapid than for discrete Gaussian disorder on a 1D lattice (blue dotted line), $D(\epsilon)/D(0) = \exp(-\beta^2\epsilon^2)(1+\mathrm{erf}(\beta\epsilon/2))^{-1}$ [6]. This makes physical sense, because energetic 'traps' caused by the proximity of nanoparticles with unusually high and low energies are geometrically harder to avoid in 1D than in 2D. The simulation result also shows a more rapid

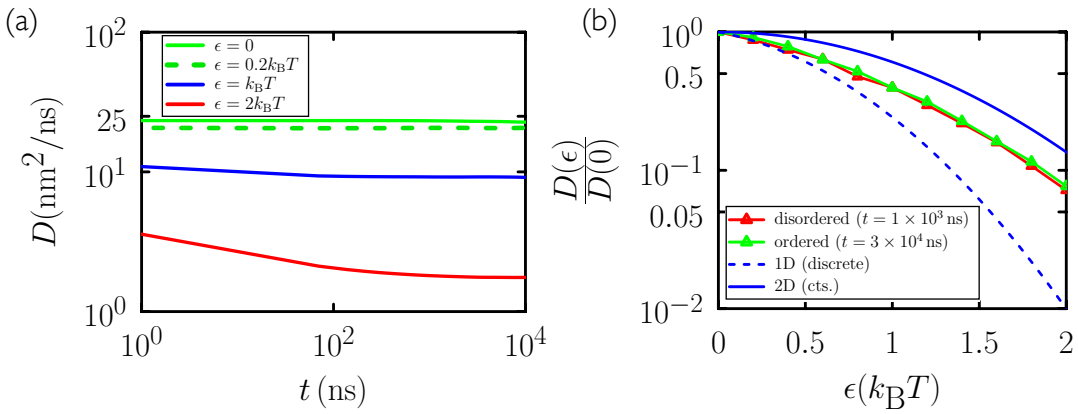

FIG. S12: (a) The diffusion parameter (S27) as a function of time, for four different values of energetic disorder (on a triangular lattice). A constant value indicates diffusive motion, which is reached at times that increase as the roughness $\epsilon/(k_BT)$ of the energy landscape increases. (b) Long-time diffusion constant obtained for particular values of substrate energetic disorder, normalized by the value for no energetic disorder. For a triangular lattice (green line) the fall-off of D with $\epsilon/(k_BT)$ is less rapid than for discrete Gaussian disorder on a 1D lattice (dotted blue line), but more rapid than for a continuous Gaussian surface in 2D (solid blue line) [6]. The presence (red line) or absence (green line) of nanoparticle spatial disorder (at constant area) has little effect on the fall-off of D with energetic roughness.

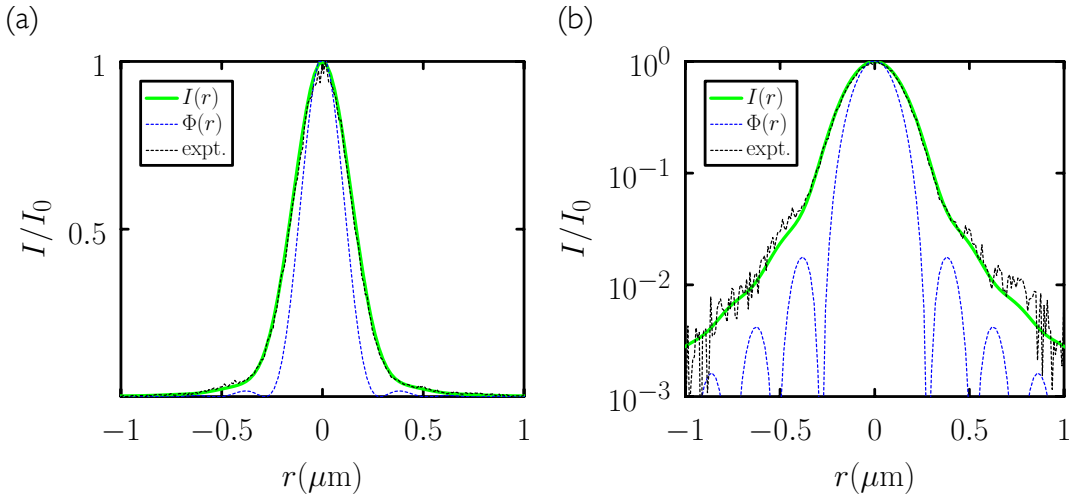

FIG. S13: The observed photoluminescence profile (black dashed line) on a sparse nanoparticle substrate is a convolution of our laser source $\Phi(r)$ (blue line), which is an Airy function with FWHM 240 nm, with the point-spread function of the optics for received light, which is an Airy function of FWHM 270 nm. The green line is the numerical convolution $I(r)$ of these two Airy functions, Eq. (S18). This convolution matches the observed profile, providing a baseline from which we can assess the effect of exciton hopping [see Supplemental Fig. S14]. Panels (a) and (b) show linear-linear and linear-log plots, respectively.

fall-off with $\epsilon/(k_BT)$ does D for a continuous Gaussian surface (solid blue line), $D(\epsilon)/D(0) = \exp(-\beta^2\epsilon^2/2)$ [6]. This hierarchy also makes physical sense: a continuous surface is less likely to give rise to particularly abrupt energy changes (traps) than are discrete energy levels drawn from a Gaussian distribution.

We found that the presence or absence of spatial disorder of nanoparticles (at constant nanoparticle areal coverage) has little effect upon $D(\epsilon)$ [compare red and green lines in Supplemental Fig. S12(b)]; the same is not true of spatial disorder at varying nanoparticle coverage, as described in Section S6.

S6. COMPARISON WITH EXPERIMENTAL DATA

In this section the parameters used in simulations are chosen to match those of our experiments. We consider a square nanoparticle grid of lattice constant 10 nm (or a continuum approximation thereof); a laser source that is an Airy profile of full width half-maximum (FWHM) 240

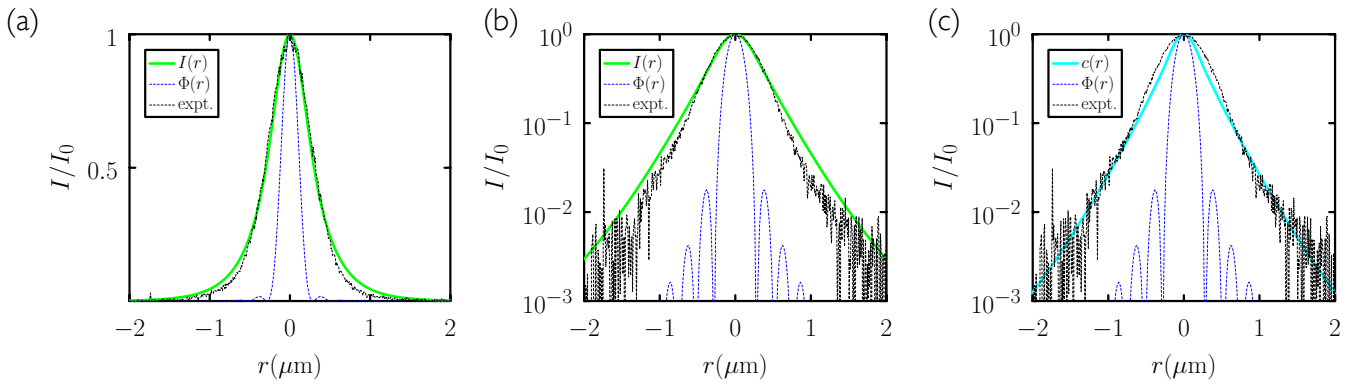

FIG. S14: The observed photoluminescence profile (black dashed line) on a dense nanoparticle substrate is broader than that shown in Supplemental Fig. S13, on account of exciton hopping. The source $\Phi(r)$ here is as in Supplemental Fig. S13. The green line $I(r)$ results from the solution $c(r)$ of Eq. (S3), for $D \approx 1\,(\mathrm{cm})^2/\mathrm{s}$, convolved with the point-spread function $S(r)$, per (S18). The scale of the broadening is consistent with that seen in experiment, supporting our estimate of the basic rate of exciton hopping. However, profile shapes are not identical, indicating that exciton hopping in experiment is not perfectly described by the diffusion equation. Panels (a) and (b) show linear-linear and linear-log plots, respectively. Panel (c) shows the exciton profile $c(r)$ (cyan line) that results from Eq. (S3) (this profile is not expected to match the experimental profile, because the latter involves convolution with the optics' point-spread function).

nm; a laser source intensity low enough that no exciton-exciton interactions occur (we are in the linear regime); a point-spread function for received light that is an Airy profile of FWHM 270 nm; and excitons of lifetime ≈ 1 ns.

In Supplemental Fig. S13 we show the experimentally measured photoluminescence profile on a sparse nanoparticle substrate (black). Here we expect the rate of exciton hopping to be effectively zero, and so we can use this case as a baseline to isolate the effect of our optics. Also shown in the figure are an Airy function of FWHM 240 nm (blue), which is the profile of the laser source on the substrate, and (in green) the convolution of this function with an Airy function of FWHM 270 nm. The latter is the point-spread function of the optics at the received wavelength. The convolution matches the observed profile, even into the tails, indicating that our optics functions as expected. Knowing this baseline is important, because it allows us to attribute the broadening of the profile seen on the dense nanoparticle substrate to exciton hopping. We show the experimentally measured photoluminescence profile on a dense nanoparticle substrate (black) in Supplemental Fig. S14. We also show the profile $I(r)$ expected for diffusive excitonic motion (green). This profile results from the exciton profile $c(r)$, calculated from Eq. (S3) in the low-power regime $\rho = 0$ for $D/\mu = 0.095\,(\mu\mathrm{m})^2$, convolved, per Eq. (S18), with the point-spread function of the optics. In that equation, $S(r)$ is an Airy function of FWHM 270 nm. The exciton profile itself is shown in cyan in panel (c). The source profile in Supplemental Fig. S14 is the same as that shown in Supplemental Fig. S13, providing a measure of the extent to which exciton hopping broadens the profile. The calculated profile shown in Supplemental Fig. S14 is consistent with the experimental result in terms of the approximate width of the profile. Taking $\mu \sim 1\,(\mathrm{ns})^{-1}$ gives $D \sim 1(\mathrm{cm})^2/\mathrm{s}$, consistent with the estimate of the exciton diffusion constant ($D \approx 0.5(\mathrm{cm})^2/\mathrm{s}$) made in the main text. In detail, however, the profiles do not match: small discrepancies can be seen in the tails – evident in the logarithmic plot of panel (b) – indicating that Eq. (S3) does not perfectly describe exciton motion on the dense substrate. In Supplemental Fig. S15 we show calculated profiles (green) for three different values of D atop experimental data: the comparison indicates that the shape of the experimental profile is not perfectly described by exciton diffusion with a single diffusion constant.

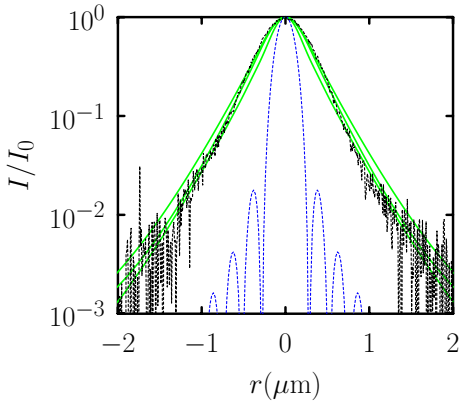

FIG. S15: As suggested by Supplemental Fig. S14, photoluminescence profiles resulting from the diffusion equation do not describe the shape of the experimental profile (black dashed line). The green lines show profiles $I(r) = (c \star S)(r)$, resulting from Eq. (S3) and Eq. (S18), for three different values of D.

The iso-energetic nature of our nanoparticles suggests

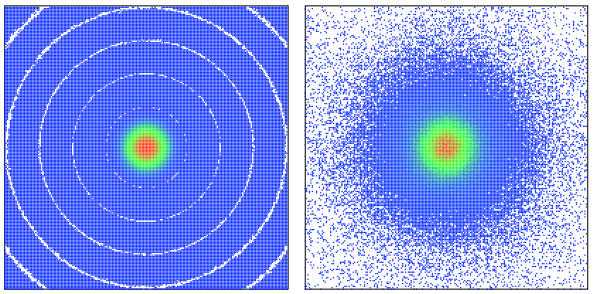

FIG. S16: Snapshots of time-averaged photon emission statistics from continuous-time Monte Carlo simulations of exciton creation and self-destruction on a square nanoparticle lattice. In the right-hand panel we also simulate exciton hopping. The laser source $\Phi(r)$ is an Airy function of FHWM 240 nm.

that exciton subdiffusion of the type seen in previous work [3] and in Section S5 B does not occur in our experiments. Instead, the presence of imperfections in the nanoparticle substrate, and the practice of averaging experimental profiles over different spatial locations, may lead to non-diffusive profiles. To investigate this possibility we turned to microscopic simulations of the kind described in Section S5 A. On a square nanoparticle lattice we simulated the processes of creation (S19), self-destruction (S20), and hopping

$$\emptyset + \mathrm{A} \overset{k}{\leftrightarrow} \mathrm{A} + \emptyset, \tag{S28}$$

using continuous-time Monte Carlo [4]. Hops were considered to any vacant nearest-neighbor nanoparticle. We assume the process of self-destruction to give rise to a photon at the same spatial location, and so the photon emission profile is the exciton profile $c(r)$ in the long-time limit. In Supplemental Fig. S16 we show example snapshots of the time-averaged photon emission statistics that result from these processes in the absence (left) and presence (right) of hopping. The source $\Phi(r)$ is again an Airy function of FWHM 240 nm; the left-hand panel is essentially an image of this function.

In Supplemental Fig. S17 we show the experimentally measured photoluminescence profile on a close-packed nanoparticle monolayer (black), together with profiles $I(r)$ (green) obtained by convolving, *via* Eq. (S18), the exciton profile $c(r)$ obtained from microscopic simulations with a point-spread Airy function $S(r)$ of FWHM 270 nm. We work in the low-power regime, with $\Phi_0/\mu = 10^{-2}$ (see Supplemental Fig. S9). Simulations done on pristine substrates match the diffusive profiles obtained using Eq. (S3). To mimic substrate imperfections we did microscopic simulations with a fraction f_V of nanoparticle vacancies. No excitons can be created on, or hop to, a vacancy. We created vacancies in a spatially uncorrelated way, which is probably not true of vacancies produced by the nanoparticle self-assembly process: there, vacancies appear to cluster as gaps. However, the effect leads to profiles with shapes similar to those seen in experiment. The value of the hopping rate k used to produce these simulations is $k/\mu = 10^3$. Taking $\mu \sim 1\,(\mathrm{ns})^{-1}$ and the nanoparticle size $a \sim 10\,\mathrm{nm}$ gives an estimate for the diffusion constant (on a pristine substrate) of $D \sim \frac{1}{2}10^3\mu a^2 \sim \frac{1}{2}\,(\mathrm{cm})^2\mathrm{s}^{-1}$. This value is consistent with the estimate derived from experimental data. The comparison of experimental and calculated profiles shown in Supplemental Fig. S17 suggests that energy transport in our experiments results from iso-energetic hopping, with a diffusion constant of order $(\mathrm{cm})^2\mathrm{s}^{-1}$, on a spatially imperfect nanoparticle substrate. The middle curve in panel (a) of Supplemental Fig. S17, produced using a vacancy fraction of 20%, is the green line in Panel (g) of the main text.

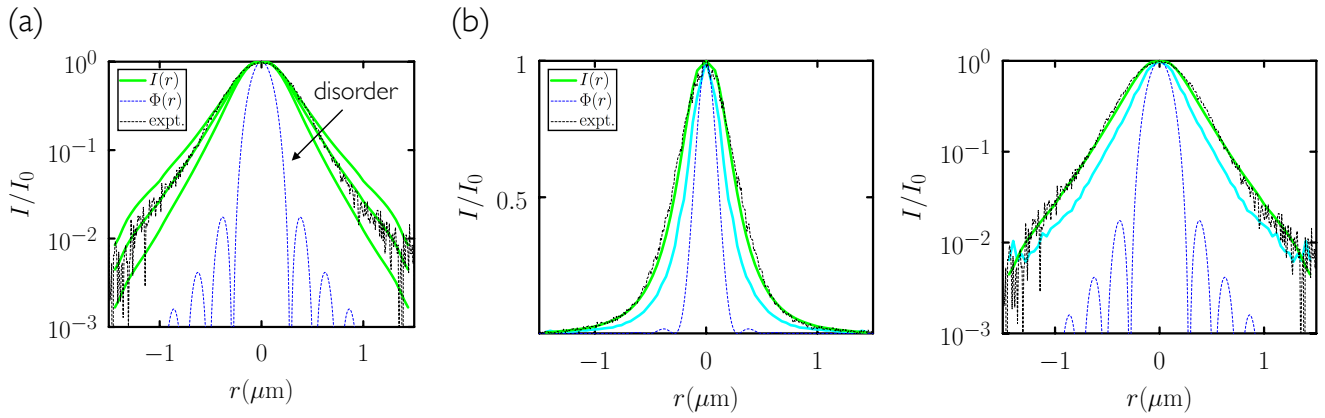

FIG. S17: Experimental photoluminescence profile (black dashed line) compared with simulated profiles $I(r) = (c \star S)(r)$ (green). The profile $c(r)$ results from continuous-time Monte Carlo simulations of exciton creation, self-destruction, and hopping; this function is convolved with $S(r)$, an Airy function of FWHM 270 nm, *via* Eq. (S18). In panel (a) we show results for parameters $\Phi_0/\mu = 10^{-2}$ and $k/\mu = 10^3$, with three different mean nanoparticle vacancy fractions f_V of 0.1, 0.2, and 0.3 (from the outside in). In panels (b) and (c) we show results for vacancy fraction 0.2 on linear-linear and linear-log plots, respectively: its shape is a better match for the experimental profile than are profiles from the diffusion equation (see Figs. S14 and S15). The cyan lines are the exciton profiles $c(r)$.

S7. ADDITIONAL EXPERIMENTAL FIGURES

- The excitation laser intensity profile is shown in Supplemental Fig. S18.
- The schematics of the optical setups are shown in Supplemental Fig. S19.
- Additional time-resolved PL spectroscopy data are provided in Supplemental Fig. S20.
- Additional lifetime measurements are provided in Supplemental Fig. S21.
- A time-resolved PL microscopy map is shown in Supplemental Fig. S22.
- The normalized PL intensity as a function of the excitation laser power is shown in Supplemental Fig. S23.

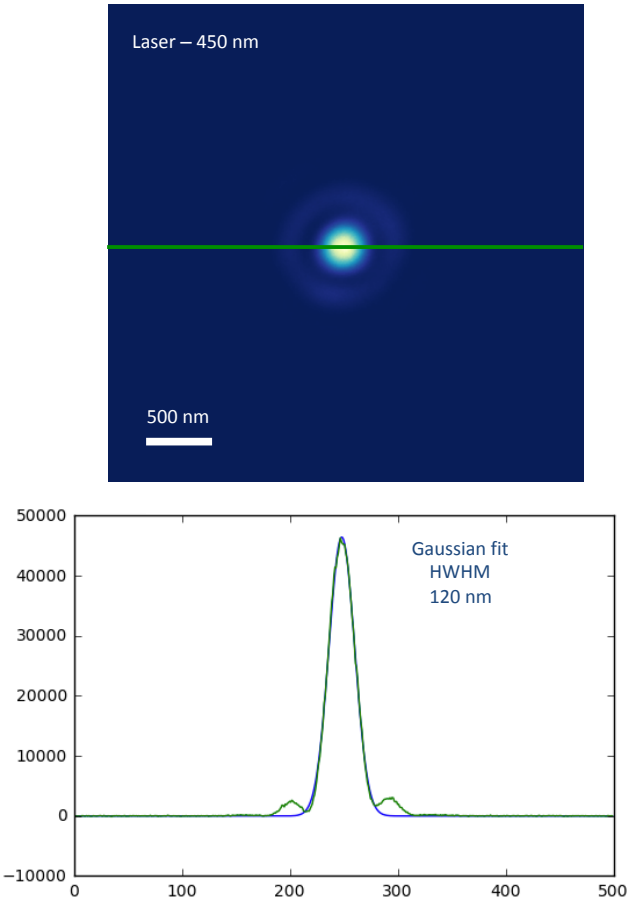

FIG. S18: (a) Diffraction limited CW laser spot (wavelength 450 nm) imaged with a CCD camera after 530X magnification. (b) Laser spot cross-section (blue) and Gaussian fit (FWHM 240 nm).

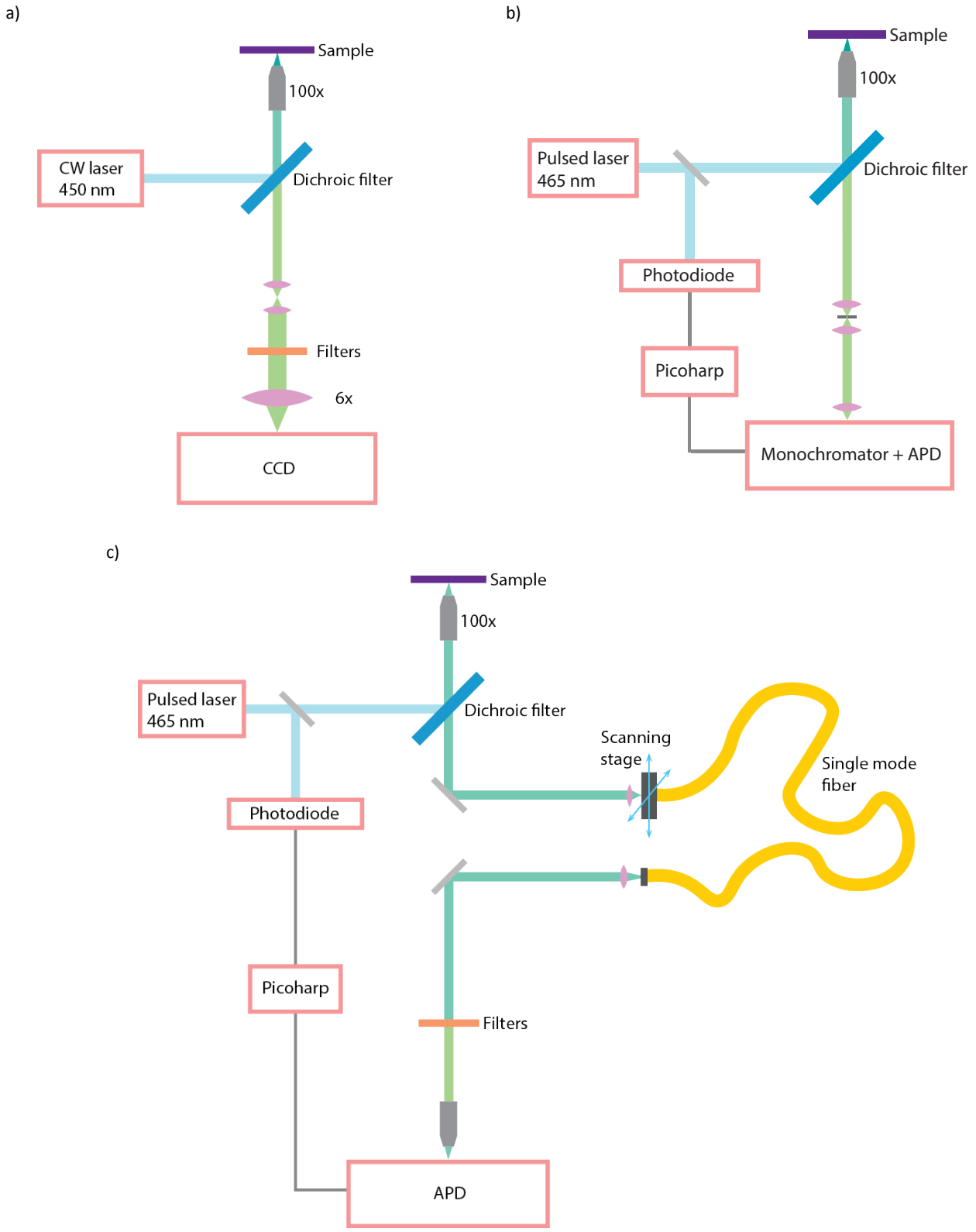

FIG. S19: Setup for (a) steady-state PL microscopy, (b) time-resolved PL spectroscopy, and (c) time-resolved PL microscopy.

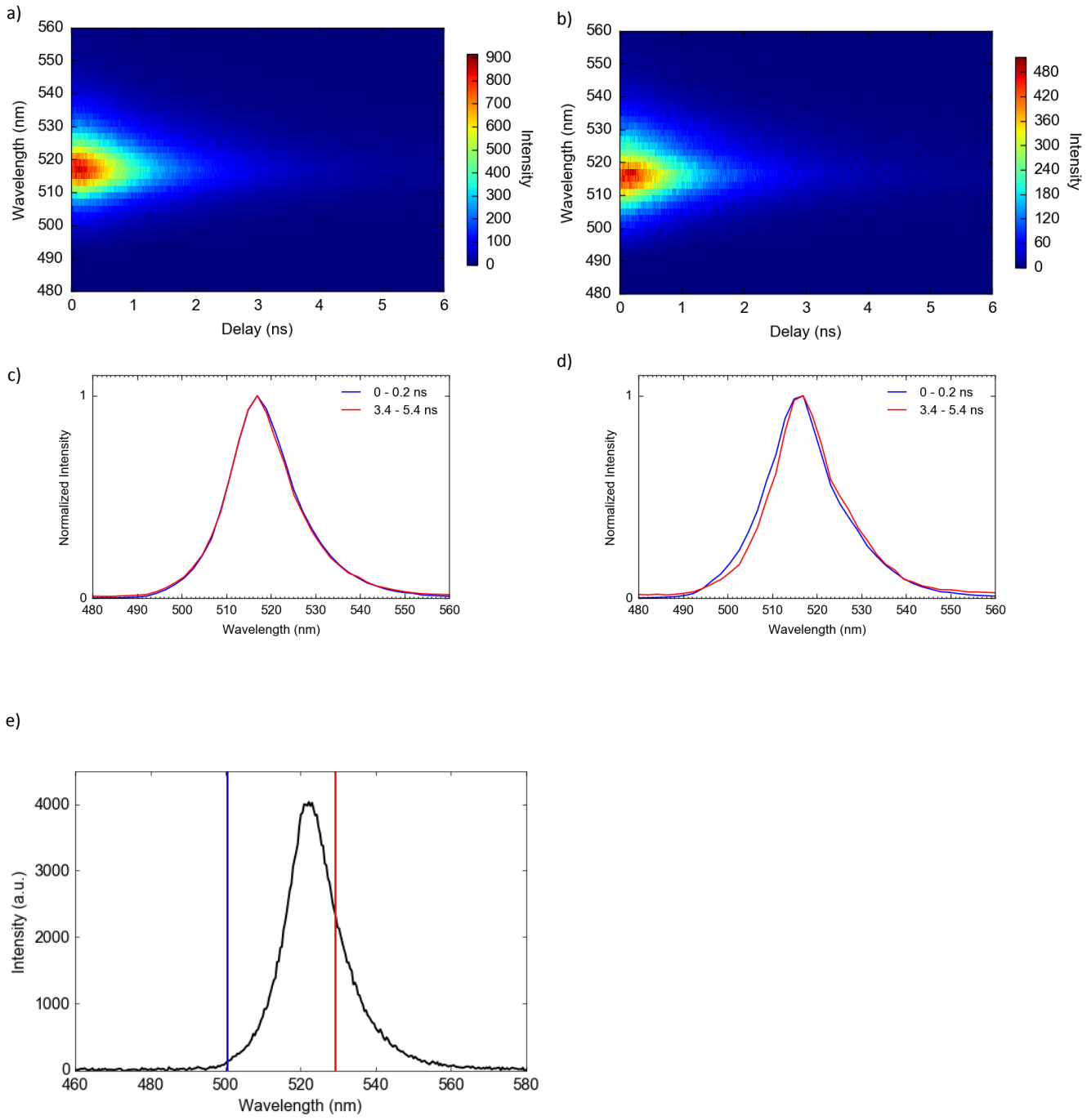

FIG. S20: Time-resolved PL spectra on (a) an ordered area made of uniformly sized PNCs and on (b) a disordered area made of PNCs of different sizes. (c) PL spectra from data in (a) integrated between 0 ns and 0.2 ns (blue) and between 3.4 ns and 5.4 ns (red). The two spectra overlap. (d) PL spectra from data in (b) integrated between 0 ns and 0.2 ns (blue) and between 3.4 ns and 5.4 ns (red). The spectrum at later time is slightly red shifted. (e) Integrated PL spectrum; the blue and red vertical lines show the PL wavelengths displayed in Figure 3-b and 3-c.

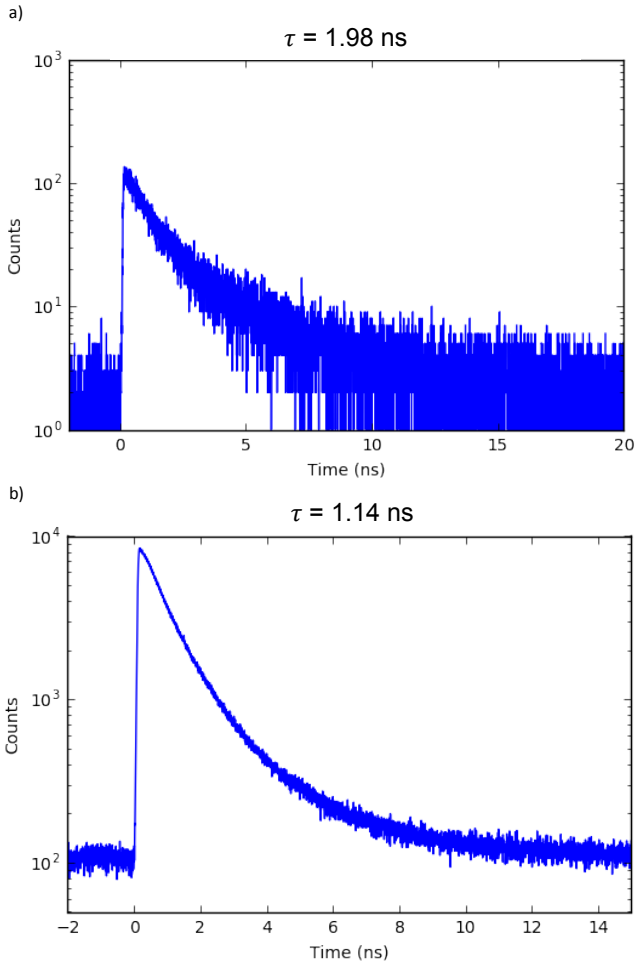

FIG. S21: Time-resolved PL of (a) PNCs assembled in a sparse monolayer; (b) PNCs assembled in a close-packed monolayer (integrated over the entire collection area). The lifetime of the system, measured as the time to reach a 37% or 1/e decay, is 1.94 ns, and 1.14 ns respectively.

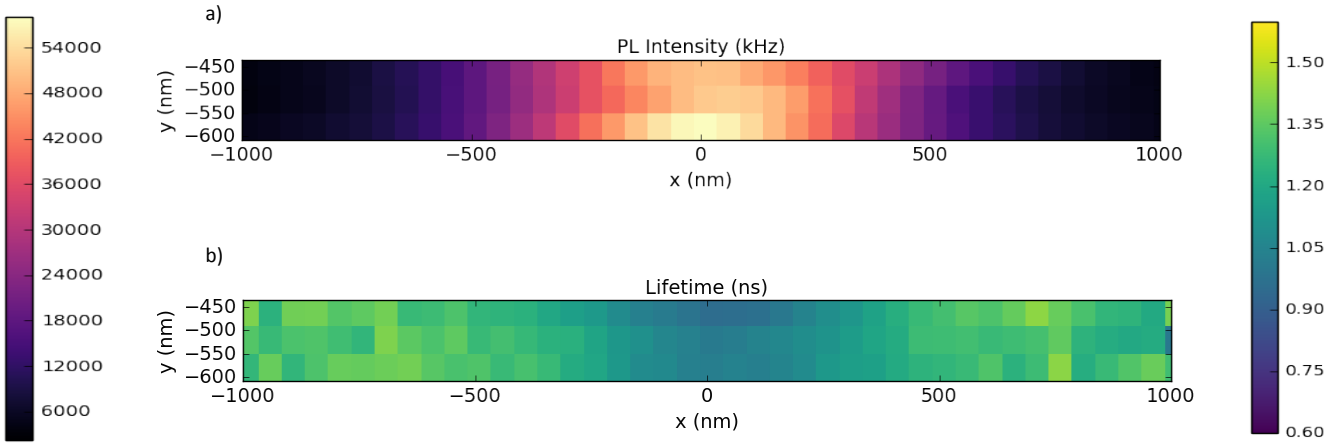

FIG. S22: (a) Time-integrated PL intensity map. (b) Lifetime map calculated from.

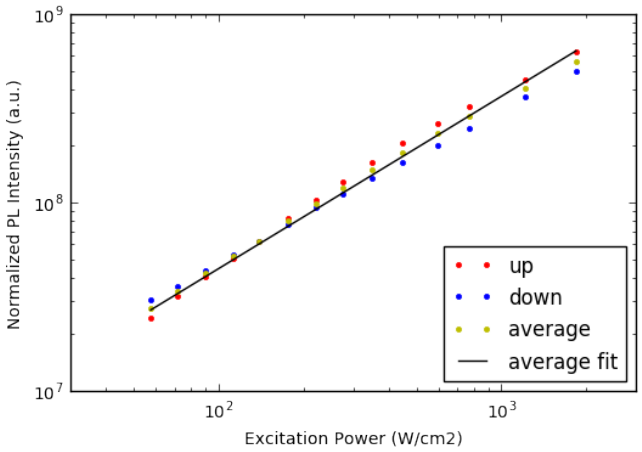

FIG. S23: Normalized PL intensity as a function of the excitation laser power. The upward scan is shown in red dots, the downward scan is shown in blue dots, and the average.

[1] Yang, J., Choi, M. K., Kim, D.-H., and Hyeon, T., Designed Assembly and Integration of Colloidal Nanocrystals for Device Application, *Adv. Mater*. **2016**, 28, 1176-1207.
[2] Hinrichsen, H., Non-Equilibrium Critical Phenomena and Phase Transitions into Absorbing States, *Adv. Phys.* **2000**, 49, 815-958.
[3] Akselrod, G. M., Prins, F., Poulikakos, L. V., Lee, E. M. Y., Weidman, M. C., Mork, A. J., Willard, A. P., Bulovic, V., and Tisdale, W. A., Subdiffusive Exciton Transport in Quantum Dot Solids, *Nano Lett*. **2014**, 14, 3556-3562.
[4] Gillespie, D. T., A General Method for Numerically Simulating the Stochastic Time Evolution of Coupled Chemical Reactions, *J. Comput. Phys.* **1976**, 22, 403-434.
[5] Zwanzig, R., Diffusion in a Rough Potential, *Proc. Natl. Acad. Sci. USA* **1988**, 85, 2029-2030.
[6] Banerjee S., Biswas, R., Seki, K., and Bagchi, B., Diffusion on a Rugged Energy Landscape with Spatial Correlations, *J. Chem. Phys.* **2014**, 141, 09B617_1.
[7] Watkins, P. K., Walker, A. B., and Verschoor G. L., Dynamical Monte Carlo Modelling of Organic Solar Cells: The Dependence of Internal Quantum Efficiency on Morphology, *Nano Lett*. **2005**, 5, 1814-1818.